Plasmons in Strongly Coupled Shock-Compressed Matter

P. Neumayer,[1,*] C. Fortmann,[1,2] T. Döppner,[1] P. Davis,[1,3] R. W. Falcone,[3] A. L. Kritcher,[1] O. L. Landen,[1] H. J. Lee,[4] R. W. Lee,[1] C. Niemann,[1,2] S. Le Pape,[1] and S. H. Glenzer[1]

[1]*Lawrence Livermore National Laboratory, Livermore, California 94551, USA*
[2]*Department of Physics and Astronomy, University of California, Los Angeles, California 90095, USA*
[3]*Department of Physics, University of California, Berkeley, California 94720, USA*
[4]*SLAC National Accelerator Laboratory, 2575 Sand Hill Road Menlo Park, California 94025, USA*

(Received 19 April 2010; published 12 August 2010)

We present the first measurements of the plasmon dispersion and damping in laser shock-compressed solid matter. Petawatt laser produced K-α radiation scatters on boron targets compressed by a 10 ns-long 400 J laser pulse. In the vicinity of the Fermi momentum, the scattering spectra show dispersionless, collisionally damped plasmons, indicating a strongly coupled electron liquid. These observations agree with calculations that include the Born-Mermin approximation to account for electron-ion collisional damping and local field corrections reflecting electron-electron correlations.

DOI: 10.1103/PhysRevLett.105.075003 PACS numbers: 52.25.Os, 52.50.Lp

Investigation of matter under shock compression in the laboratory is an important technique to study the physics of dense matter. Modeling astrophysical objects including, e.g., interiors of giant planets [1,2], low mass stars, and brown dwarfs [3,4] requires understanding of matter at pressures exceeding 1 Mbar [5,6] and temperatures of the order 1 eV [7]. These conditions are produced through interaction of energetic high power lasers with solid density targets. In addition, the quest of producing a burning fusion plasma in the laboratory [8] by compressing matter up to 1000 g/cm^3 requires accurate knowledge of the equation of state [9,10], thermodynamic [11] and transport properties [12], as well as static and dynamic structure of matter under such extreme conditions.

Spectrally resolved x-ray scattering has been shown to measure the microscopic physical properties of dense matter [13]. Proof-of-principle experiments in isochorically heated beryllium [14] have observed plasmons (longitudinal electron plasma oscillations, Langmuir waves) in forward-scattering geometry yielding electron density and temperature when applying the Born-Mermin approximation (BMA) [15] to calculate the plasmon energy shift and damping. Subsequent measurements in shock-compressed matter have provided density data consistent with the width of Compton scattering [16]. Also, plasmon measurements were successful in determining compression and ionization in coalescing shocks [11].

In these nearly Fermi degenerate systems reached by shock compression, electron-ion collisions solely determine the plasmon width for small momentum transfers $\mathbf{k}$, where noncollisional (Landau) damping is suppressed [17], and the plasmon width is a direct measure of the optical conductivity. This is different from dilute plasmas, e.g., space or magnetic fusion plasmas, where Landau damping dominates over collisional damping.

Also, k-vector resolved measurements of the plasmon resonance energy will reflect electron-electron interactions that will affect the dispersion in the vicinity of the Fermi momentum. Theoretical models for the dynamical structure factor $S_{ee}(k, \omega)$, result in vastly different dispersions. The random phase approximation (RPA) as well as the BMA accounting for electron-ion collisions predict a parabolic (Bohm-Gross) dispersion [18,19]. Plasmon dispersion data deviating from the RPA have been observed in cold metals [20–22]. In shock-compressed matter, the decrease of the plasmon dispersion due to electron-electron local field effects will occur simultaneously with electron-ion collisions affecting plasmon damping.

In this Letter we present the first frequency and k vector resolved plasmon spectra from shock-compressed matter. Boron samples have been compressed by interaction with high energy laser pulses, resulting in conditions above solid density, electron density $n_e = 4 \times 10^{23}$ cm^{-3}, at moderate temperature, $k_B T_e = 0.2$ eV. When the shock front has reached the rear surface of the target, resulting in a homogeneously compressed sample, the plasma conditions have been probed by laser produced K-α radiation at two energies (5 keV and 8 keV) under various scattering angles $31° < \theta < 68°$. The source size and acceptance angle of the spectrometer lead to an accuracy of $\pm 10\%$ for the scattering angles. While experimental spectra in the limits of small and large k vectors provide independent measurements of the plasma conditions, we further observe a horizontal plasmon dispersion in the range of wave vectors between $k = 1.7$ Å^{-1} and 2.0 Å^{-1}. These results agree with theoretical predictions for $S_{ee}(k, \omega)$ within the extended Born-Mermin approximation (BMA). This model includes electron-electron correlations via the local field correction factor (LFC) [23] and electron-ion collisions via the dynamical electron-ion collision frequency [24]. These effects account for differences of 3 eV in plasmon width and 10 eV in shift when compared to the RPA resulting in significant corrections for applications of x-ray Thomson scattering to plasma diagnostics.

The experiment, carried out at the Jupiter Laser Facility at LLNL uses rectangular slabs of 2×3 mm^2 solid boron (α phase, mass density $\rho_0 = 2.46$ g/cm^3), polished down to a thickness of 170 μm. A schematic of the setup is shown in Fig. 1(a). A 2ω (527 nm) drive laser with energy of 400 J compresses the boron samples in a 10 ns-long flat top pulse. The laser radiates the target at an angle of 37.5° to the target normal with a homogeneous intensity profile applying a 700 μm continuous phase plate providing for a planar shock front to propagate into the target. Figure 1(b) shows results of radiation-hydrodynamic simulations using the code HELIOS [25] indicating homogeneous mass density ($\rho = 3.8$ g/cm^3) and pressure ($p = 1.8$ Mbar) profiles at the end of the drive. The electron temperature rises from $k_B T_e = 0.2$ eV in the shock front to approximately 1 eV at 10 μm behind the drive side.

Ultrashort pulse laser produced K-α radiation probes the compressed boron plasma by x-ray Thomson scattering. Energies of 250 J are delivered at a pulse duration of 10 ps and at 1053 nm wavelength, yielding intensities of $\approx 10^{17}$ W/cm^2. Vanadium and copper foils of 10 μm thickness provide K-α photon energies of 4.95 and 8.05 keV, respectively, with k vectors between $k = 1.3$ Å^{-1} and $k = 4.3$ Å^{-1}, on separate target experiments.

X-rays scattered by the dense plasma disperse in a cylindrically bent 70×25 mm^2 large graphite crystal (highly oriented pyrolitic graphite) and are focused in a von Hamos setup onto an imaging plate detector (Fujifilm). A 100 μm thick gold shield blocks the direct view of the spectrometer crystal to the intense x-ray probe source. The gold shield has been coated with several μm CH to avoid Au emission induced by stray light.

Figure 2 shows experimental and theoretical plasmon scattering data from shock-compressed B. The data at small momentum transfer show a strong plasmon resonance downshifted by 32 eV from the K-α probe energy of 4.95 keV, see Fig. 2(a). This feature is 1 order of magnitude stronger compared to scatter from uncompressed targets, indicating the presence of a large fraction of free electrons due to shock induced ionization, which is consistent with earlier compression experiments using the diamond anvil-cell technique [26]. With increasing momentum transfer k the plasmon is increasingly damped, and in the proximity of the Fermi momentum the plasmon energy is constant, Fig. 2(b). These observations agree with calculations for the DSF at an electron density of $n_e = 4 \times 10^{23}$ cm^{-3}. The calculations apply the newly devel-

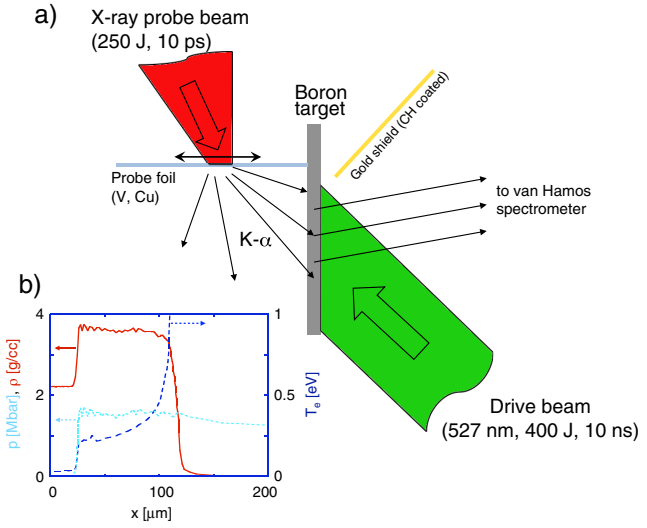

FIG. 1 (color online). (a) Schematic of the experiment showing the drive beam that compresses boron and the x-ray probe beam that is delayed by 10 ns producing the x-ray probe radiation. The probe foil material and probe laser position on the foil is varied to access a range of k vectors. (b) Mass density, electron temperature, and pressure as function of target depth at $t = 10$ ns from HELIOS simulations. The irradiated surface is located at $x = 200$ μm.

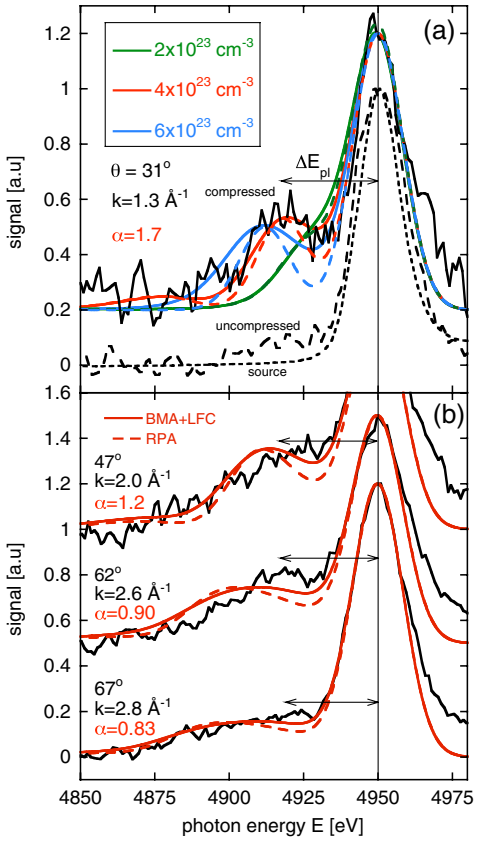

FIG. 2 (color online). (a) X-ray scattering spectra (solid black) from compressed targets at 31° scattering angle compared to fit calculations using BMA + LFC (solid colored) and the RPA (dashed colored) for three different densities. Also shown are the V probe spectrum (dotted) and scattering from uncompressed targets (black dashed). (b) Scattering spectra for $\theta = 47°$, 62°, and 67° and fit calculations using BMA + LFC (solid) and RPA (dashed). Arrows indicate the experimental plasmon shift $\Delta E(k)$; $\alpha = \kappa_{\mathrm{TF}}/k$ is the scattering parameter with the Thomas-Fermi inverse screening length $\kappa_{\mathrm{TF}} = (m_e e^2/\pi\epsilon_0\hbar^2)^{1/2}(3n_e/\pi)^{1/6}$.

oped BMA + LFC model for $S_{ee}(k, \omega)$ [27],

$$S_{ee}(k, \omega) = \frac{\hbar k^2 n_B(\omega)}{\pi m_e \omega_{\mathrm{pl}}^2} \mathrm{Im}\left[\frac{\frac{z}{i\nu(\omega)}\chi_e(k, z)\chi_e(k, 0)}{\chi_e(k, z) + \frac{\omega}{i\nu(\omega)}\chi_e(k, 0)}\right], \quad (1)$$

where $\omega_{\mathrm{pl}} = \sqrt{n_e e^2/\epsilon_0 m_e}$ is the plasma frequency, and $n_B(\omega)$ is the Bose function. Furthermore $z = \omega + i\nu(\omega)$ with $\nu(\omega)$ being the complex valued collision frequency. The latter is calculated within second order perturbation theory (Born approximation) and in the long wavelength limit, $k \to 0$ [24]. At finite transfer momentum, also electron-electron interactions have to be considered. Their influence on the dynamical structure factor is described by the local field correction (LFC) $G(k)$ in the electron one-component plasma response function,

$$\chi_e(k, \omega) = \frac{\chi_e^{(0)}(k, \omega)}{1 - V(k)[1 - G(k)]\chi_e^{(0)}(k, \omega)}. \quad (2)$$

$\chi_e^{(0)}(k, \omega)$ is the electronic RPA response function, see, e.g., Ref. [28], $V(k) = e^2/\varepsilon_0 k^2$ is the Coulomb potential in wave number representation. For the LFC, we use the parametrization by Farid *et al.* [29], supported by Monte Carlo simulations of dense electron liquids [30]. Our treatment of correlations in the electron OCP is consistent with the hydrodynamic simulations. HELIOS uses the SESAME tabulated equation of state, the electronic contribution is obtained from a Thomas-Fermi-Dirac model where exchange and correlations are treated within the local density approximation [31].

Roots in the denominator of Eq. (2) lead to plasmon resonances observed in the scattering spectrum. Since $G(k) > 0$, the LFC factor gives a decrease of the plasmon resonance position. Also, $G(k)$ scales as k^2 at wave numbers $k \ll k_F$, $k_F = (3\pi^2 n_e)^{1/3}$ being the Fermi wave number. Consequently, for conditions of Fig. 2(a) the plasmon energy shift is only weakly influenced by the LFC. In this limit the plasmon energy shift in BMA + LFC agrees with the values obtained in the RPA.

Figure 2(a) shows calculations for BMA + LFC and RPA for three electron densities indicating sensitivity of the plasmon shift to n_e. The plasmon shift, $\Delta E_{\mathrm{pl}} = (32 \pm 3)$ eV, yields $n_e = (4.0 \pm 0.7) \times 10^{23}$ cm^{-3}. We determine the ionization $Z_f = 2.3$ from the noncollective signal at 4.3 Å^{-1} by comparing the integrated inelastic scatter to the elastic part [32]. From n_e and Z_f we deduce the mass density $\rho = 3.2$ g/cm^3, corresponding to $\rho/\rho_0 = 1.3$.

Figure 2(b) shows that the experimental plasmon shift (arrows) is constant within an error bar of 5 eV. The plasmon shift is the separation between the x-ray probe energy and the maximum of the spectrum after subtraction of the ion feature. This behavior is consistent with the BMA + LFC calculations and indicate increasing local field effects due to strong electron coupling ($\Gamma \simeq 1.4 r_s = 2.5$, $r_s = [3/4\pi n_e a_B^3]^{1/3}$ is the Brueckner parameter) [33].

Since $k_B T_e \simeq 0.2$ eV, we deal with a Fermi degenerate plasma, $k_B T_e/E_F = 0.01$, the Fermi energy is $E_F = \hbar^2 k_F^2/2m_e = 19.8$ eV. In this regime, the plasmon spectrum is not sensitive to T_e.

Figure 3(a) shows the experimental results for $\Delta E_{\mathrm{pl}}(k)$ compared to the RPA and BMA with and without local field corrections. In the limit $k \to 0$, all three models converge towards the plasma frequency, in agreement with the data. With increasing k the experimental dispersion is constant at $\Delta E_{\mathrm{pl}}(k) \simeq 33$ eV. The plasmon group velocity $v_G = d\omega(k)/dk$ vanishes, i.e., plasmons do not propagate at this energy. This behavior is in good agreement with the fully collisional BMA + LFC calculation but contradicting the RPA as well as the usual BMA that neglects the LFC factor [18].

In the strongly noncollective regime, the BMA + LFC calculation quickly converges into the single particle dispersion (Compton shift $\Delta E_C = \hbar^2 k^2/2m_e$), as expected and consistent with the RPA and the usual BMA. In this limit correlations become less important since distances smaller than the screening length are probed. Within the

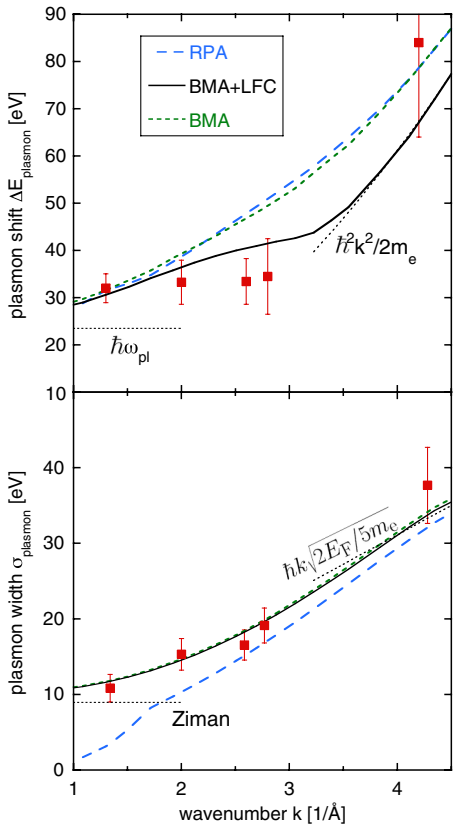

FIG. 3 (color online). Plasmon dispersion (a) and rms width (b) as function of the scattering wavevector k. Experimental data are compared to RPA (blue dashed), BMA with LFC (solid black) and BMA without LFC (green small dashes) calculations. The black dotted lines represent the limits of dispersion and damping at small and large k, respectively.

error margins, all three models are consistent with the noncollective scattering data at $k = 4.3$ Å^{-1}.

Finally, we analyze the plasmon rms width as a function of k, results are shown in Fig. 3(b) and compared to RPA and BMA with and without local field corrections. Instrumental and source broadening (cf. the source spectrum in Fig. 2) have been subtracted. Error bars are determined by varying the rms width of a fit function within a 5% confidence interval around the central value. The two points at $k = 1.3$ Å^{-1} and 2.0 Å^{-1} corresponding to collective scattering show that plasmon damping is mainly due to electron-ion collisions. Conversely, the RPA underestimates the plasmon width.

At the present density, the critical wave number up to which plasmons are a well-defined mode is $k_c = 1.7$ Å^{-1}. Above k_c, the plasmon merges with the single-pair continuum [17] giving rise to Landau damping in the RPA theory. At $k = 1.3$ Å^{-1}, we find the plasmon resonance at $\Delta E_{\mathrm{pl}} = 32$ eV, which lies beyond the cutoff energy of the single-pair continuum $\hbar\omega_{\mathrm{pair}} \leq \hbar^2(k^2 + 2kk_F)/2m_e = 29.1$ eV. The sharp edge of the pair continuum reflects the steplike Fermi distribution of degenerate electrons. Hence, within the RPA, the plasmon mode cannot couple to the single-pair continuum and therefore is undamped.

At 47° scattering angle, $k = 2.0$ Å^{-1}, the plasmon appears at $E_{\mathrm{pl}} = 33$ eV, which is within the single-pair continuum $\hbar\omega_{\mathrm{pair}} \leq 50.1$ eV. Hence, Landau damping is finite, explaining the increased spectral width in the RPA calculation as compared to the 31° case. However, RPA still underestimates the plasmon damping, whereas we obtain good agreement using the BMA + LFC model.

We also show the Ziman result [34] as the asymptotic limit of collisional damping as $k \to 0$. In the Compton scattering regime ($\alpha < 1$), where the width approaches that of the Compton profile $\sigma_C = \hbar k\sqrt{2E_F/5m_e}$ both RPA and BMA agree and are consistent with the data.

In conclusion, we demonstrated k-vector and frequency resolved x-ray Thomson scattering on plasmons in shock-compressed matter. Our data show very good agreement with the fully collisional BMA + LFC model for the dynamical structure factor. The calculations explain the plasmon broadening due to electron-ion collisions as well as vanishing plasmon dispersion due to strong electron-electron coupling. In the limits of small and large k vectors, we observe the well-known analytical limits for the plasmon dispersion and damping.

We have successfully modeled the scattering from a strongly coupled, degenerate, yet moderately hot electron-ion plasma, where thermal effects (e.g., Landau damping) start to compete against quantum degeneracy. This is important for the understanding of matter under even more extreme conditions encountered in near future inertial confinement fusion experiments, where both compression and temperature are much higher than in our case, such that the competition between thermal and quantum behavior is still an important issue.

This work was performed under the auspices of the U.S. Department of Energy by Lawrence Livermore National Laboratory under Contract No. DE-AC52-07NA27344 and supported by LDRD grant 08-ERI-002. C. F. acknowledges the Alexander von Humboldt Foundation.

*Present address: GSI, 64291 Darmstadt, Germany.

[1] G. Chabrier, Plasma Phys. Controlled Fusion **51**, 124014 (2009).
[2] N. Nettelmann *et al.*, Astrophys. J. **683**, 1217 (2008).
[3] A. Burrows *et al.*, Rev. Mod. Phys. **65**, 301 (1993).
[4] A. Burrows *et al.*, Astrophys. J. **345**, 939 (1989).
[5] D. G. Hicks *et al.*, Phys. Rev. B **79**, 014112 (2009).
[6] M. Koenig *et al.*, Plasma Phys. Controlled Fusion **47**, B441 (2005).
[7] P. M. Nilson *et al.*, Phys. Rev. E **79**, 016406 (2009).
[8] J. Lindl *et al.*, Phys. Plasmas **11**, 339 (2004).
[9] M. D. Knudson *et al.*, Science **322**, 1822 (2008).
[10] D. K. Bradley *et al.*, Phys. Rev. Lett. **102**, 075503 (2009).
[11] A. L. Kritcher *et al.*, Science **322**, 69 (2008).
[12] V. E. Fortov *et al.*, Phys. Rev. Lett. **99**, 185001 (2007).
[13] S. H. Glenzer *et al.*, Rev. Mod. Phys. **81**, 1625 (2009).
[14] S. H. Glenzer *et al.*, Phys. Rev. Lett. **98**, 065002 (2007).
[15] R. Redmer *et al.*, IEEE Trans. Plasma Sci. **33**, 77 (2005).
[16] H. J. Lee *et al.*, Phys. Rev. Lett. **102**, 115001 (2009).
[17] D. Pines *et al.*, *The Theory of Quantum Liquids* (Benjamin, New York, 1966), Vol. 1.
[18] R. Thiele *et al.*, Phys. Rev. E **78**, 026411 (2008).
[19] D. Bohm *et al.*, Phys. Rev. **75**, 1851 (1949).
[20] W. Schülke *et al.*, Phys. Rev. B **33**, 6744 (1986).
[21] W. Schülke *et al.*, Phys. Rev. B **54**, 17 464 (1996).
[22] B. C. Larson *et al.*, Phys. Rev. Lett. **77**, 1346 (1996).
[23] K. Utsumi and S. Ichimaru, Phys. Rev. B **23**, 3291 (1981).
[24] H. Reinholz *et al.*, Phys. Rev. E **62**, 5648 (2000).
[25] J. J. MacFarlane *et al.*, J. Quant. Spectrosc. Radiat. Transfer **99**, 381 (2006).
[26] M. I. Eremets *et al.*, Science **293**, 272 (2001).
[27] C. Fortmann, A. Wierling, and G. Röpke, Phys. Rev. E **81**, 026405 (2010).
[28] N. R. Arista and W. Brandt, Phys. Rev. A **29**, 1471 (1984).
[29] B. Farid *et al.*, Phys. Rev. B **48**, 11 602 (1993).
[30] S. Moroni, D. M. Ceperley, and G. Senatore, Phys. Rev. Lett. **75**, 689 (1995).
[31] S. Lyon *et al.*, LANL, Report No. LA-UR-92-3407, 1992.
[32] S. Le Pape *et al.*, Phys. Plasmas **17**, 056309 (2010).
[33] In degenerate systems $\Gamma(E_F r_s)^{-1} \propto r_s$, instead of $(Tr_s)^{-1}$ as in classical plasmas.
[34] G. Röpke *et al.*, Phys. Rev. E **60**, R2484 (1999).